CHAPTER 04 Experimentation of A-TIG welding

4.1 Preamble

To perform the autogenous TIG welding and A-TIG welding, a welding fixture is used as discussed in chapter 3. To identify the working range of process parameters and select the fluxes trial experiments are performed. After identifying the range of selected process parameters A-TIG welding process was performed on 2205 Duplex Stainless Steel (DSS). By varying welding current, torch speed and flux systematic experiments are performed to analyze the effect on weld morphology, microstructure and mechanical properties of welded joints. Experiments results indicate that oxide flux (TiO_2, SiO_2 and Cr_2O_3) increases the weld penetration as well as exhibits the higher mechanical strength of weld metal. A good correlation between the microstructure and mechanical properties is observed. To improve and enhance the performance of weld, the identification of adequate welding conditions (optimum variables) is very essential. For predicting the responses (depth of penetration (DOP), bead width, tensile strength and microhardness) mathematical models are generated for a given set of input variables using Response Surface Methodology (RSM). The multi-objective optimization is performed by applying the desirability approach to obtain the desired responses. Experimental validation is performed at multi objective optimized parameters to check the adequacy of the proposed optimized tool.

4.2 A-TIG welding trial experiments

Activated TIG welding has been carried out to form a butt joint of $100 \times 100 \times 6$ mm AISI 2205 Duplex stainless steel plate. All work piece edges are grind by the surface grinder and the plate top surface is cleaned with acetone to remove the impurities. As discussed in chapter 3 to perform A-TIG welding SiO_2, TiO_2, Cr_2O_3, MoO_3 oxide flux are selected. The amount of flux used per run is shown in Table 4.1. Before welding, the SiO_2 flux is mixed with acetone (8 mm per gm of flux) and stirred well using a stirrer to form paint-like consistency. This flux is coated on a weld surface with a paint brush as shown in Figure 4.1. To ensure the 0.15 mm flux coating thickness entire quantity of flux is deposited.
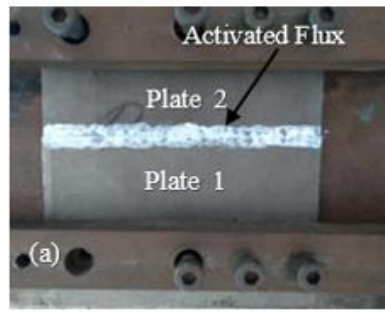
Figure 4.1 Flux applied in A-TIG welding

Table 4.1 Quantity of flux required for experimentation

Oxide Flux	Density of flux (gm/mm^3)	Length (mm)	Width (mm)	Height (mm)	Acetone (ml)	Weight of flux (gms)
Cao	0.0035	100	12	0.15	5.04	0.63
Cr_2O_3	0.00522	100	12	0.15	7.51	0.939
SiO_2	0.00265	100	12	0.15	3.81	0.477
TiO_2	0.00423	100	12	0.15	6.09	0.761
Al_2O_3	0.00395	100	12	0.15	5.68	0.711
MoO3	0.00469	100	12	0.15	6.75	0.844
CuO	0.00631	100	12	0.15	9.08	1.135

To identify the working range of welding current and torch speed experiments are performed at different combinations of two variables. Trial experiments are performed at: (i) minimum current with maximum speed, (ii) maximum current and minimum speed and (iii) average welding current and torch speed. The trial experiments are performed for all these three conditions with four selected fluxes (SiO_2, TiO_2, Cr_2O_3, MoO_3). The selected range of parameters for trial experiments is shown in Table 4.2.

Table 4.2 A-TIG Welding parameters

Sr. No.	Welding parameters	Selected Value
1.	Current	120-185- 250A when the gas flow rate is 12 l/min
2.	Shielding gas flow rate	12 l/min
3.	Shielding gas	Argon
4.	Vertex angle of electrode	45^0
5.	Torch speed	100-120-140 mm/min

6.	Electrode	Thoriated Tungsten (EWTh-2) diameter (d) 2.5 mm
7.	Conical length of electrode	3 mm
8.	Torch angle	90^0
9.	Flux	SiO_2, TiO_2, Cr_2O_3 , MoO_3
10.	Arc length	2mm

The weld metal samples under the different weld conditions are shown in Figure 4.2,4.3 and 4.3. It is observed (experiment no. 4) that MoO_3 flux creates a greater amount of slug on the weld surface and makes the weld surface undesirable. Moreover, to identify the working range of variable macrostructure study is performed as shown in Table 4.3.

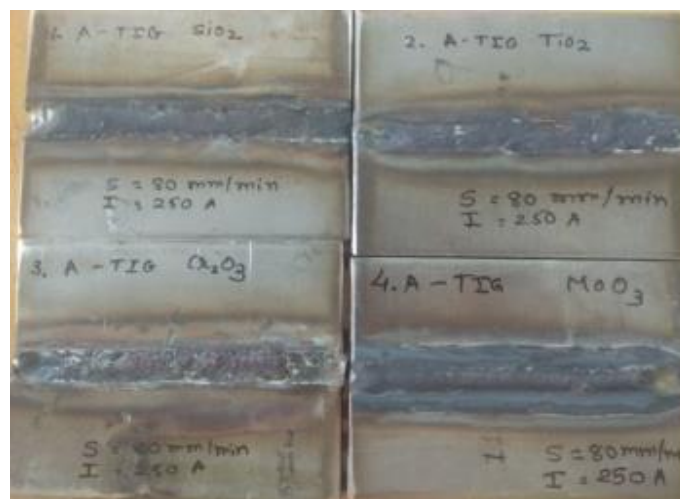Figure 4.2 Welding current: 120 A, Torch speed 200 mm/min

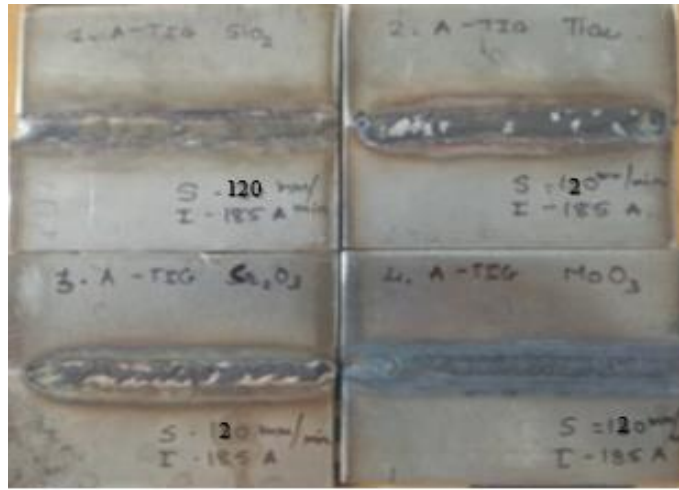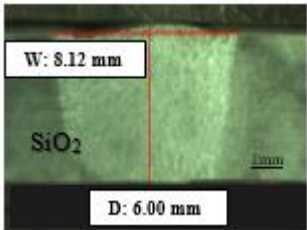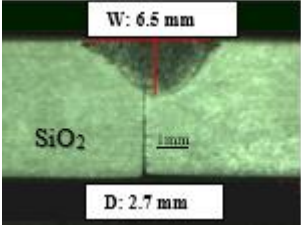Figure 4.3 Welding current: 250 A, Torch speed 80 mm/min

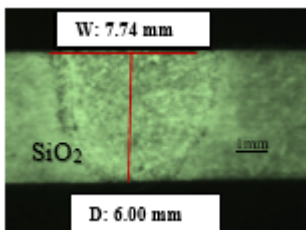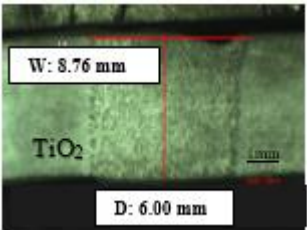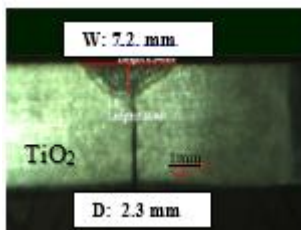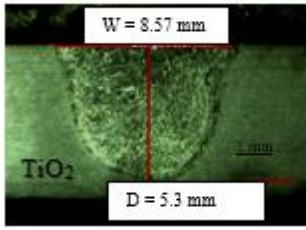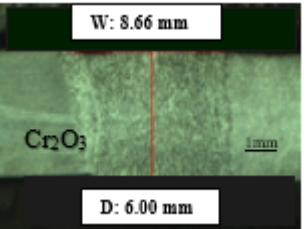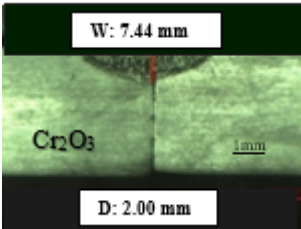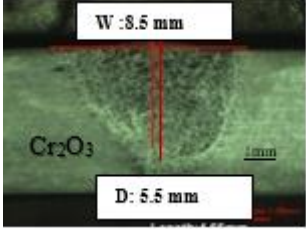Figure 4.4 Welding current: 185 A, Torch speed 120 mm/min

Table 4.3 A-TIG weld bead geometry

Welding current 250 amps, Torch speed 80 mm/min	Welding current 120 amps, Torch speed 200 mm/min	Welding current 185 amps, Torch speed 120 mm/min
W: 8.12 mm, SiO₂, D: 6.00 mm	W: 6.5 mm, SiO₂, D: 2.7 mm	W: 7.74 mm, SiO₂, D: 6.00 mm
D/W: 0.73	D/W: 0.41	D/W: 0.77
W: 8.76 mm, TiO₂, D: 6.00 mm	W: 7.2 mm, TiO₂, D: 2.3 mm	W = 8.57 mm, TiO₂, D = 5.3 mm
D/W: 0.68	D/W: 0.31	D/W: 0.61
W: 8.66 mm, Cr₂O₃, D: 6.00 mm	W: 7.44 mm, Cr₂O₃, D: 2.00 mm	W: 8.5 mm, Cr₂O₃, D: 5.5 mm
D/W: 0.69	D/W: 0.26	D/W: 0.65

54

| D/W: 0.68 | D/W: 0.24 | D/W: 0.52 |
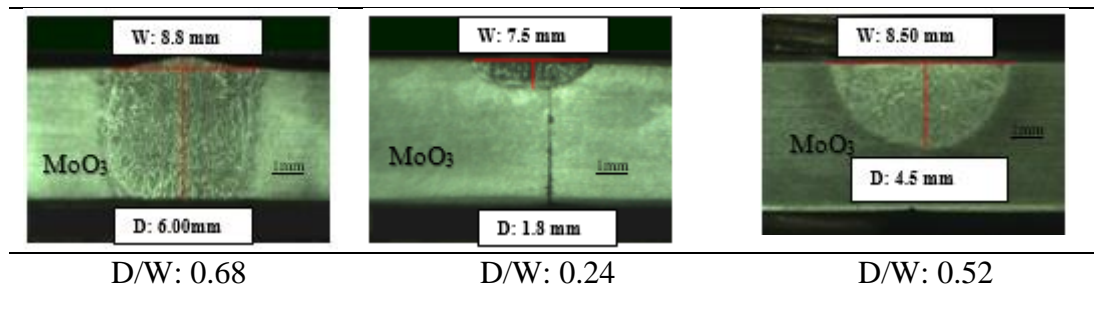
With MoO$_3$ flux poor penetration is reported in minimum and average conditions as well MoO$_3$ flux destroys the weld bead appearance. Therefore, in the final experiments, MoO$_3$ flux is not considered. High torch speed and welding current make the weld pool wider thereby increasing the bead width. Similarly, low torch speed and welding current create the shallow weld pool. Therefore, to perform the final experiments average variable range is selected as shown in Table 4.4.

Table 4.4 Variable parameters range

Sr. No.	Variable welding parameters	Selected working range
1.	Welding Current	160-185-210 amps
2.	Torch speed	100-120-140 mm/min
3.	Flux	SiO$_2$, TiO$_2$, Cr$_2$O$_3$

4.2 Experimentation of A-TIG Welding

Grade 2205 DSS plates were cut in size of $100 \times 100 \times 6$ mm, polished using silicon carbide paper and the rust is removed by cleaning with acetone before the butt welding. In the present study input variables such as welding current, torch speed and flux which predominantly affect weld bead geometry are identified by trial and error approach as aforementioned in Table 4.4. The other constant parameters such as shielding gas, flow rate, arc length, etc. are already mentioned in Table 4.2. Before the experiments, activated flux is mixed with acetone and applied a thin layer of flux on the surface to be butt weld. The coating thickness is maintained at 0.15 mm throughout the weld line.

The quality of the weld strongly depends upon the selection of process variables. To obtain the desired response and to reduce the number of experiments trial design of the experiment (DOE) approach is introduced. RSM is one form of DOE that was introduced in 1950 by Box and Wilson (1960). RSM is a statistical technique to develop the mathematical model which gives the relationship between the input and output variables and also predicts the

response for the set of input variables within a limit (Ibrahim & Elkhidir, 2011). Box-Behnken designs (BBD) approach of RSM is the most appropriate design approach for the three-level factorial design (Vora, Abhishek, & Srinivasan, 2019). In the present study, the BBD approach is implemented for the three selected input variables and their level for RSM is mentioned in Table 4.5. The formulated design matrix is shown in Table 4.6.

Table 4.5 Welding variables and their level for RSM

Parameters	Units	Factor levels		
		-1	0	1
Current (I)	Amps	160	185	210
Torch speed (S)	mm/min	100	120	140
Flux	-	SiO_2	TiO_2	Cr_2O_3

Table 4.6 Box-Behnken Design Matrix for selected welding parameters

Run	Welding current (amps)	Torch speed (mm/min)	Flux
1	185	120	TiO_2
2	185	140	Cr_2O_3
3	210	120	Cr_2O_3
4	160	140	TiO_2
5	185	120	TiO_2
6	210	140	TiO_2
7	185	120	TiO_2
8	185	120	TiO_2
9	160	100	TiO_2
10	210	120	SiO_2
11	185	120	TiO_2
12	210	100	TiO_2
13	160	120	SiO_2
14	185	140	SiO_2
15	160	120	Cr_2O_3
16	185	100	Cr_2O_3
17	185	100	SiO_2

Furthermore, experiments are conducted as per the design matrix and the A-TIG butt-welded plates are shown in Figure 4.5. All A-TIG welded samples top surface is found to be smooth and continuous without any spatter along the weld line. However, the entrapped flux particles form the slug along the weld line.

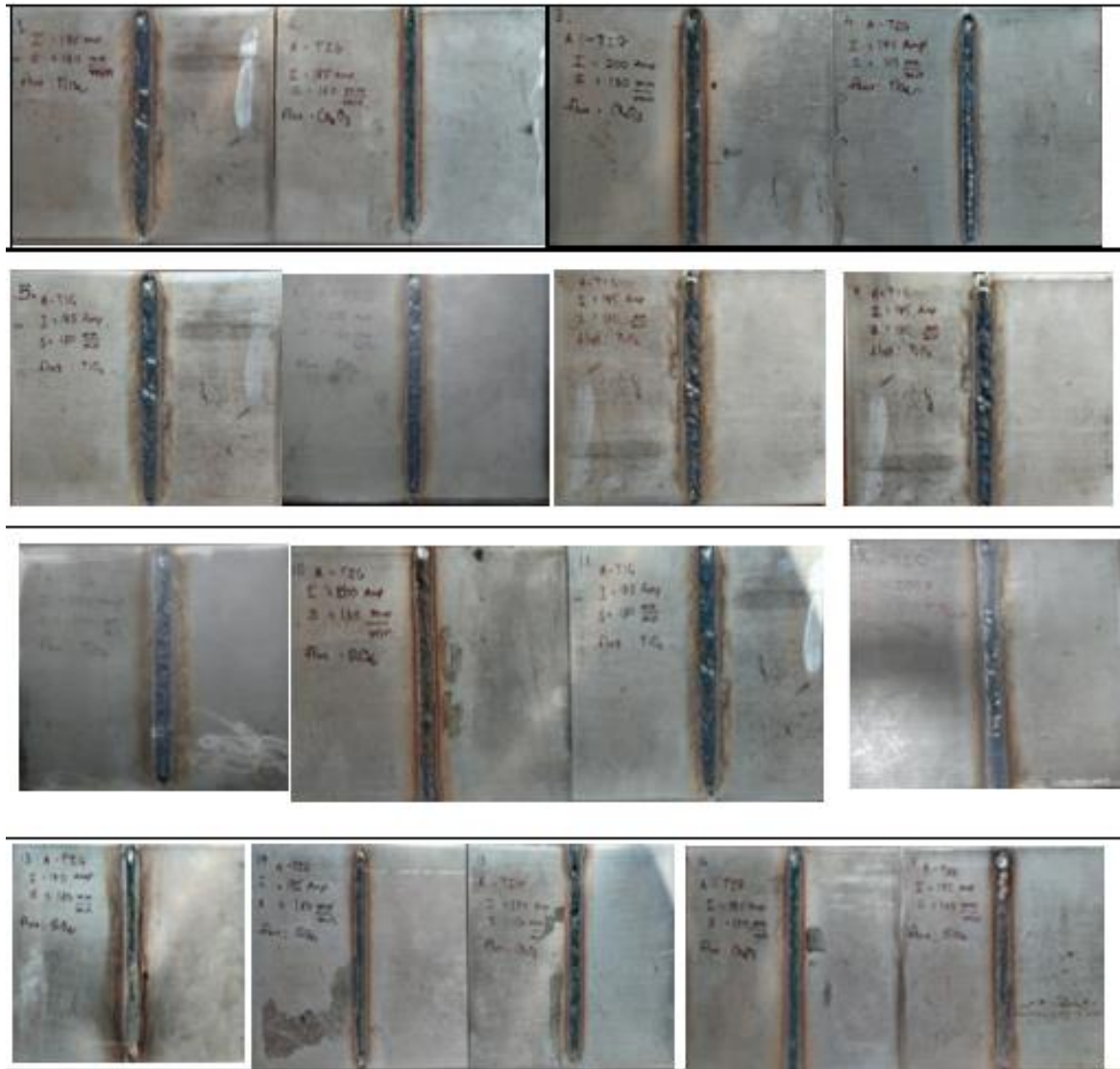Figure 4.5 A-TIG welded specimen as per design matrix

4.3 Investigation of Metallurgical and Mechanical property

The subsequent subsections cover a comparison of TIG and A-TIG 2205 DSS weld metal, weld bead geometry, microstructure which are further followed by mechanical properties.

4.3.1 Weld bead characteristics

The macrostructure of weld bead geometry of A-TIG and TIG 2205 DSS weldments are

shown in Figure 4.6 and Figure 4.7 respectively. The variation in geometry is also measured in terms of the D/W ratio. The TIG weld penetration is reported as 2.02 mm with 12.9 mm bead width (D/W: 0.15) at 185 amps current and 100 mm/min weld speed (Figure 4.7). Whereas, full penetration is reported in A-TIG welding with a reduction in bead width compare to TIG weld. The macro graphic observation shows that an activated flux greatly affects the weld bead appearance. The resultant macrostructure of A-TIG weld metal shows the full and secure weld penetration with the highest d/w ratio (0.87) at the same TIG weld parameters. The higher penetration depth in A-TIG welding is due to reversal Marangoni convection and arc constriction mechanisms.
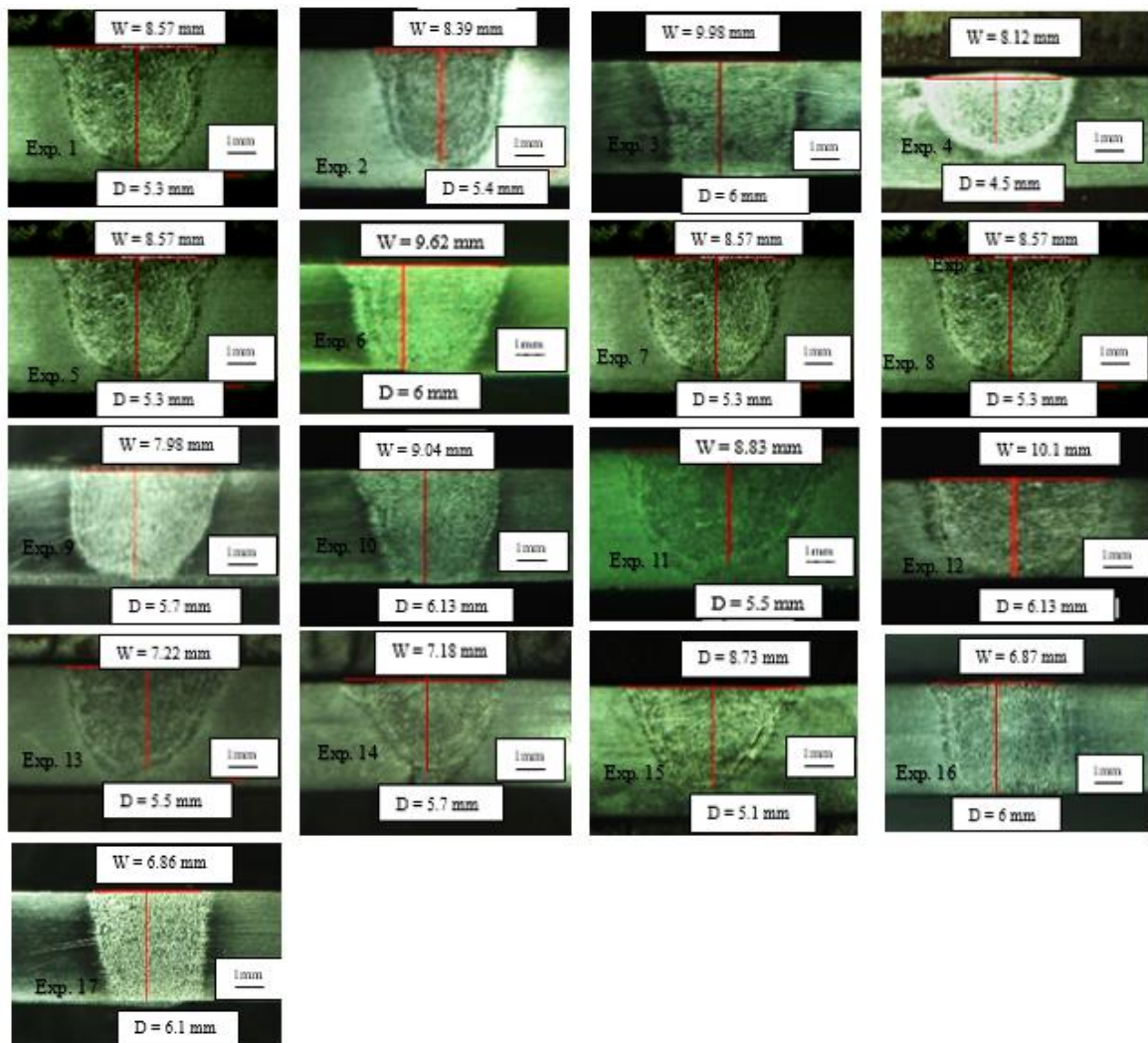

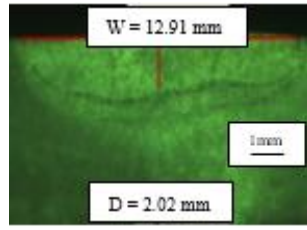Figure 4.6 Macrostructure of A-TIG 2205 DSS weld metal

Figure 4.7 Macrostructure of TIG 2205 DSS weld metal

4.2.2 Microstructure

The variation in the microstructure of TIG and A-TIG welded 2205 DSS has been investigated. The base metal microstructure of 2205 DSS as shown in Figure 4.8(a) indicates the islands of austenite phase (grey color) in a matrix of ferrite (black color). TIG weld microstructure shows (weld current 185 amp and torch speed 100 mm/min)) that the grains of austenite and dendritic delta ferrite phase are uniformly distributed and form uniform grain boundary in weld metal (Figure 4.8 (b)). The welded 2205 DSS weld pool first solidified as delta ferrite phase and later stage in austenitic phase due to the significant amount of molybdenum and chromium (ferrite stabilizers) present in the base metal (Tathgir, Rathod, & Batish, 2019). In TIG weld metal ferrite content increased to 79 FN from its initial value of 62 FN as demonstrated in Figure 4.8 (b). During the TIG welding, weldment cools very rapidly therefore the transformation of ferrite to the austenite phase is not able to complete which results in a large amount of ferrite forms in 2205 DSS after the solidification which is well in the agreement with other researchers (Chern, Tseng, & Tsai, 2011; Muthupandi, Bala Srinivasan, Seshadri, & Sundaresan, 2003)
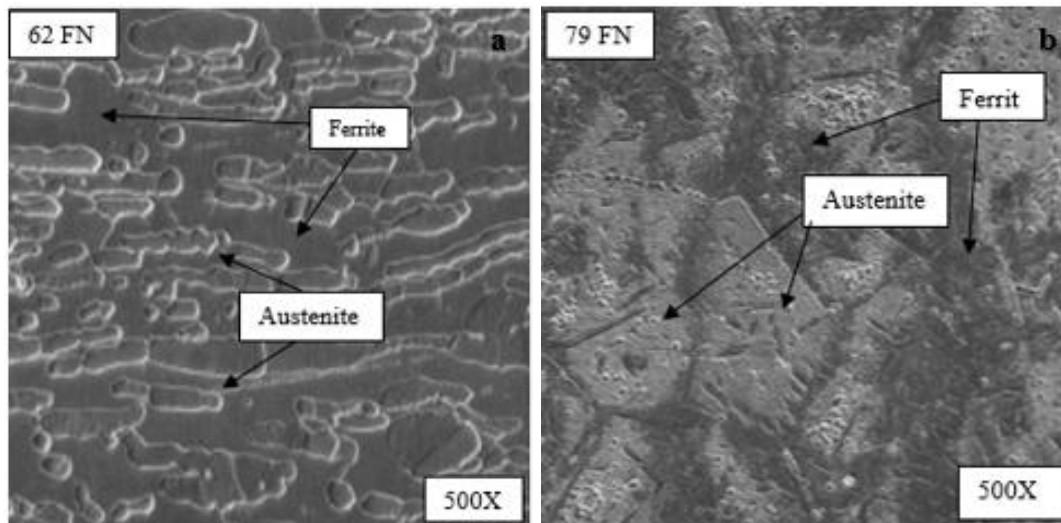

Figure 4.8(a) Parent metal microstructure (b) TIG weld metal microstructure of 2205 DSS

59

Similarly, the HAZ zone of A-TIG weld metal is shown in Figure 4.9 (a),(b) at different weld conditions. When DSS cool at room temperature the different form of austenite such as wedge-shaped Widmanstätten austenite, grain boundary austenite and intergranular precipitates forms in the ferrite matrix of A-TIG weld metal. The intergranular austenite observed near the region separated by Widmanstätten austenite. Muthupandi et al. (2003) also reported similar observations. Sindu Kuo (2002) reported that Widmanstätten austenite and grain boundary austenite formed at high temperatures whereas intergranular austenite formed at a lower temperature because it required higher driving force for precipitation. The ferrite content in A-TIG weld under the different welding conditions is 73 FN and 76 FN with SiO_2 flux as shown in Figure 4.9which is lower than TIG weld this attributes to total heat input form during the welding process.
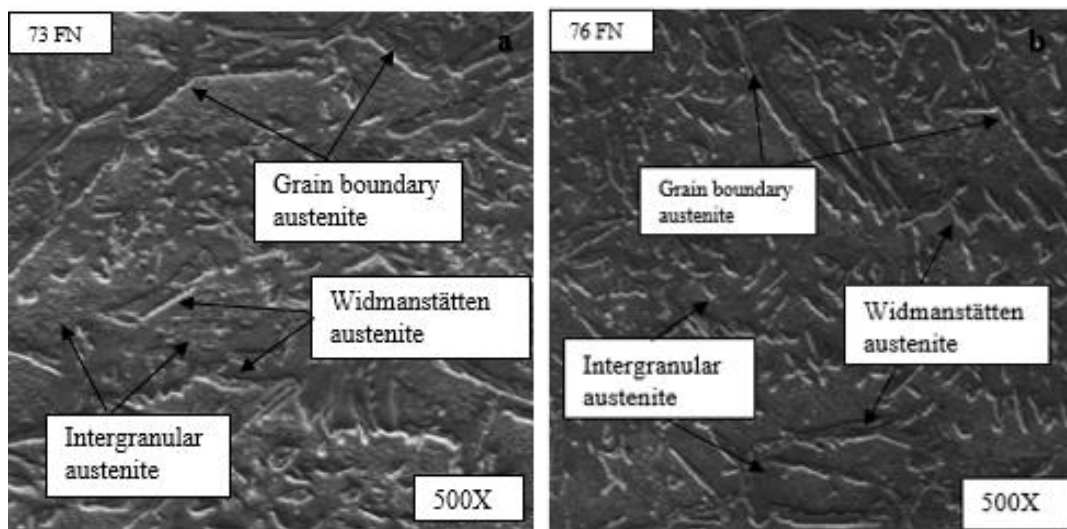
Figure 4.9 A-TIG, 2205 DSS weld metal at (a)185 amps current and 100 mm/min torch speed SiO_2 flux (b)160A current, 140 mm/min torch speed, TiO_2 flux

In A-TIG welding applied flux increases the heat input and peak temperature of weld metal. During A-TIG welding, the cooling rate is reduced and transformation of delta ferrite to austenite can complete at the equilibrium stage. This results in lower ferrite in 2205 DSS compared to TIG weld. Similar, observation is reported by Chen et al. (2011). Therefore, heat input is the key factor that affects the ferrite phase in the weld metals after solidification.

4.2.3 Tensile strength

To understand the effect of process variables on mechanical properties, tensile tests are performed on TIG and A-TIG welded 2205DSS. The tensile study attested that all

weldments failures accrue at the fusion zone in all cases (Figure 4.10). The reason behind the weld zone failure is the formation of coarsening ferrite grains with Widmanstätten austenite during the solidification of A-TIG weld. After TIG welding with single-pass, tensile strength is reported 690Mpa (Table 4.7) which is less than base metal strength (720MPa. The reduction in tensile strength is due to low heat input, faster cooling rate and formation of a large amount of delta ferrite (79 FN). Tensile strength in A-TIG butt weld metal is also not satisfactory in a few cases which is due to incomplete penetration as shown in Table 4.8

Figure 4.10 Failed tensile test specimen of A-TIG 2205 Duplex stainless steel weld

Table 4.7 Experimental results of TIG weld

Current (Amp)	Torch speed (mm/min)	DOP (mm)	BW (mm)	D/W	Tensile strength (MPa)	Microhardness (HV)
185	100	2.02	12.91	0.15	690	362

Table 4.8 Experimental results of A-TIG weld

Sr. No	Current (Amp)	Torch speed (mm/min)	Flux	DOP (mm)	BW (mm)	Tensile strength (MPa)	Average Microhardness (HV)
1	185	120	TiO_2	5.3	8.57	590	290
2	185	140	Cr_2O_3	5.4	8.39	660	305
3	210	120	Cr_2O_3	6	9.98	720	289
4	160	140	TiO_2	4.5	8.12	560	355
5	185	120	TiO_2	5.3	8.57	590	290

6	210	140	TiO$_2$	6	9.62	745	330
7	185	120	TiO$_2$	5.3	8.57	590	290
8	185	120	TiO$_2$	5.3	8.57	590	290
9	160	100	TiO$_2$	5.7	7.98	600	300
10	210	120	SiO$_2$	6.13	9.04	752	305
11	185	120	TiO$_2$	5.5	8.83	576	299
12	210	100	TiO$_2$	6.13	10.1	700	287
13	160	120	SiO$_2$	5.5	7.22	595	335
14	185	140	SiO$_2$	5.7	7.18	715	333
15	160	120	Cr$_2$O$_3$	5.1	8.73	600	338
16	185	100	Cr$_2$O$_3$	6	6.87	730	325
17	185	100	SiO$_2$	6.1	6.86	760	320

However, with 185-amp current, 100 mm/min torch speed and SiO$_2$ flux highest joint efficiency [(UTS weld/UTS base metal) x 100] 105 % is reported. This is attributed highest D/W ratio (0.87) and less delta ferrite (73FN) than TIG weld (79FN) as shown in Figures 5 (a) and 4 (b) respectively. Other researchers also achieved higher tensile strength with SiO$_2$ flux in duplex stainless steel (Devendranath, et al., 2015). Moreover, higher tensile strength in A-TIG weld is attributed to Widmannstetter structure formation with high miss-orientation of grain in A-TIG weld metal zones. Which shows a good correlation between the microstructure and tensile properties.

4.3.3 Microhardness

The microhardness of parent metal and weld metal depends on the amount of austenite and ferrite present in the weldment microstructure. Higher microhardness exhibited in ferrite phase than austenite phase owing to the presence of more amount of molybdenum and chromium atoms (Jebaraj & Ajaykumar, 2017). However, the study attested that variation in austenite and ferrite ratio did not lead to many variations in hardness (Jebaraj & Ajaykumar, 2017). This is because substitution elements do not have sufficient time for partitioning of alloying substances during the cooling of weld. Therefore, less variation in ferrite and austenite phase was reported and leads to similar hardness in DSS (Gunn, 1997). However, the excessive ferrite phase is also responsible for higher hardness. Variation in heat input significantly affects the hardness of 2205 DSS weld. It was reported that higher the heat input leads to slow the cooling rate and larger the grain size with a high amount of

austenite which reduces the hardness of DSS weldments (Jana, 1992).

A Vickers microhardness (100 gm load) on the traverse weld region of TIG and A-TIG welds are depicted in Table 4.7 and Table 4.8. In all A-TIG weld conditions, fusion zones exhibit microhardness in the range of 290-355HV. TIG weld microhardness (185 A current and 100 mm/min torch speed) is 362 HV which is higher than all A-TIG weld metals. This attributes to lower the heat input faster cooling rate than A-TIG weldments and higher amount of ferrite phase (79 FN) in TIG weld metal.

Variation in microhardness in A-TIG weld with different parameters are not significantly fluctuating. However, in A-TIG weld metal microhardness are higher than base metal this is due to higher ferrite than the base metal. Moreover, in A-TIG weld metal Widmanstätten secondary austenite structure is observed since previously deposited weld metal reheats which are responsible for higher microhardness of weldment. Highest micro hardness 355 HV is obtained at 160 amps welding current, 140 mm/min torch speed, and TiO_2 flux in A-TIG weld.

4.4 Development of mathematical model

To test the results (weld bead geometry, mechanical properties) of A-TIG welded 2205 DSS mathematic models are built up. The design matrix represented in Table 4.6 is statistically analyzed using Design Expert 13 software by applying RSM. The empirical relationships were derived in form of process variables i.e. welding current, torch speed, flux for predicting the four responses i.e. depth of penetration, bead width, tensile strength and microhadness of A-TIG weld joint. The adequacy of the developed model is verified by F value of lack of fit test and Analysis of Variance (ANOVA) method to get the perfect fit model. Second-order regression equations are generated to represent responses.

4.4.1 Development of a mathematical model for depth of penetration

The adequacy of the developed mathematical model is analyzed by using the Analysis of Variance (ANOVA). A generated model is measured to be significant if the p-value is less than 0.05. The Design expert software is used to measure the significance level of the regression model and lack of fit. The developed model for depth of penetration has a p-value (significance probability value) is less than 0.05. This indicates that the developed model has a 95% significance level as shown in Table 4.9. Along with this, the F-value of lack of fit is insignificant. The R^2 and adjusted R^2 values are 0.9647 and 0.9436

63

respectively, which is near to 1 and thus confirms the adequacy of the model. ANOVA results show the adequate precision value is 24.7248 which indicates the signal-to-noise ratio. If this ratio is found to be greater than 4, then it represents the adequacy of the model. Figure 4.11 shows the plot of actual and predicted depth of penetration. As represented in Table 4.9, the predicted R^2 is near to the actual R^2. Thus, Figure 4.11 and R^2 value together represent that the developed model is accurate enough to predict the DOP. The derived forward regression mathematical model for depth of penetration in terms of process parameters is shown by equation 4.1.

Depth of penetration (DOP) = 21.35716 - 0.0469 × I - 0.22351 × S + 1.3476 × flux + 0.000535 × I × S + 0.000458 × S² - 0.31602 × flux²   (4.1)

Table 4.9 ANOVA analysis for depth of penetration

| Source	Sum of Squares	df	Mean Square	F-value	p-value	Source
Model	3.08	6	0.5127	45.61	< 0.0001	significant
A-A	1.5	1	1.5	133.14	< 0.0001	
B-B	0.6786	1	0.6786	60.38	< 0.0001	
C-C	0.0771	1	0.0771	6.86	0.0256	
AB	0.2862	1	0.2862	25.47	0.0005	
B²	0.1418	1	0.1418	12.62	0.0052	
C²	0.2933	1	0.2933	26.1	0.0005	
Residual	0.1124	10	0.0112			
Lack of Fit	0.0804	6	0.0134	1.67	0.3214	not significant
Pure Error	0.032	4	0.008			
Cor Total	3.19	16		R²	0.9786	
	Std. Dev.	0.199	0.1060	Adjusted R²	0.9436	
	Mean	8.4	5.59	Predicted R²	0.8785	
	C.V. %	2.37	1.90	Adequate Precision	26.9276	
				R²	0.9786	
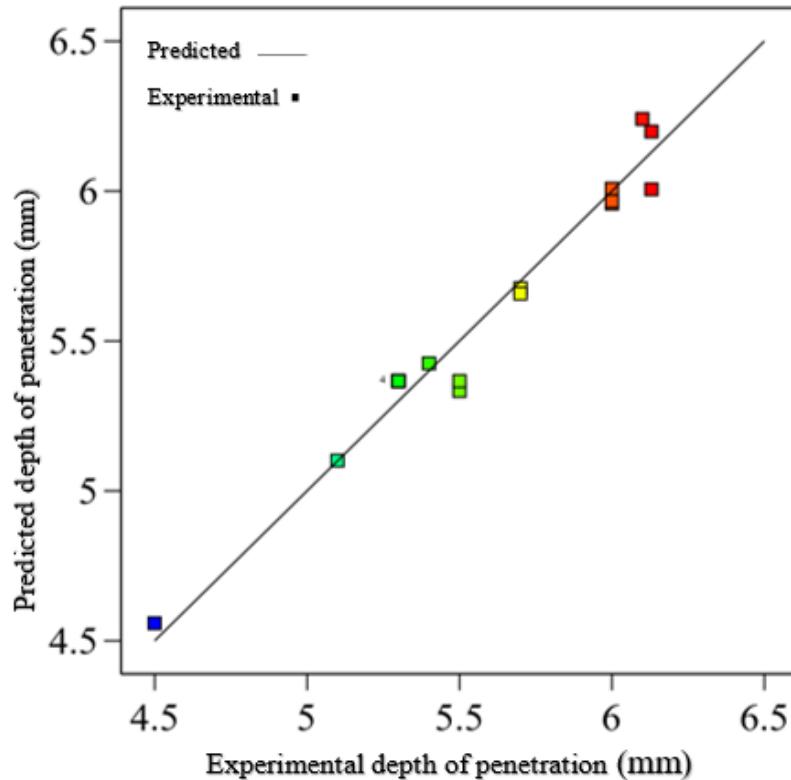
Figure 4.11 Schematics illustration of predicted values and experimental values agreement of depth of penetration

4.4.2 Development of a mathematical model for bead width

The ANOVA analysis for bead width is conducted and discussion is given below (Table 4.10). The bead width of the developed model has a p-value which is significant and F value of the Lack of fit value is found insignificant. The R^2 and adjusted R^2 value are 0.9718 and 0.9499 respectively, which is near to unity which confirms the adequacy of the model. Moreover, the adequate precision value is 23.0703 of the ANOVA result. width shows the plot of actual and predicted bead width. As represented in Table 4.10, the predicted R^2 is near to the actual R^2. Thus, Figure 4.12 and R^2 value together represent that the developed model is accurate enough to predict the bead width. The derived forward regression mathematical model for bead width in terms of process parameters is shown by equation 4.2.

Bead width (BW) = 37.63821 - 0.492838 × I + 0.307668 × S - 6.98818 × flux + 0.021091 × S × flux + 0.001422 × I² - 0.001390 × S² + 1.09300 × flux² (4.2)

Table 4.10 ANOVA analysis for bead width

| Source	Sum of Squares	df	Mean Square	F-value	p-value	Source
Model	15.44	7	2.21	44.33	< 0.0001	significant
A-A	5.59	1	5.59	112.43	< 0.0001	
B-B	0.6781	1	0.6781	13.63	0.0019	
C-C	0.2417	1	0.2417	4.86	< 0.0001	
BC	0.9307	1	0.9307	18.70		
A²	3.33		3.33	66.87		
B²	1.30	1	1.30	26.16	< 0.0001	
C²	3.51	1	3.51	70.48	< 0.0001	
Residual	0.4478	9	0.0498			
Lack of Fit	0.3938	5	0.0788	5.82	0.0655	not significant
Pure Error	0.0541	4	0.0135			
Cor Total	15.89	16				
Std. Dev.			0.2231	Adjusted R²	0.9499	
Mean			8.42	Predicted R²	0.8632	
C.V. %			2.65	Adequate Precision	23.0703	
				R²	0.9718	
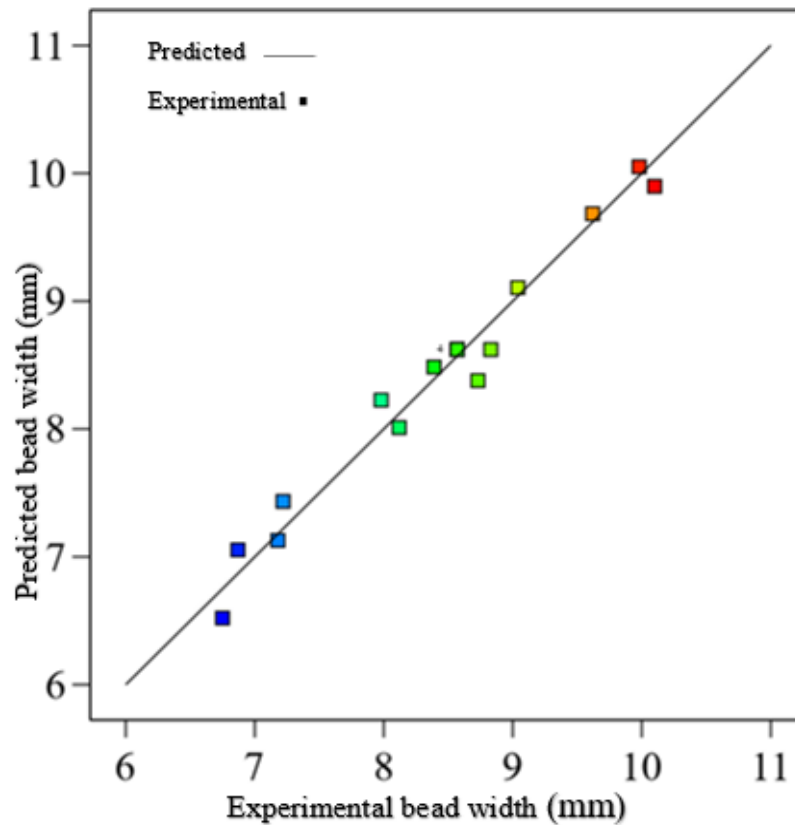
Figure 4.12 Schematics illustration of predicted values and experimental values agreement of bead width

4.4.3 Development of a mathematical model for tensile strength

The ANOVA analysis for tensile strength is performed and discussion is given below. The developed model of tensile strength has a p-value is less than 0.05 as shown in Table 4.11. The F value of Lack of fit is found to be insignificant. The R^2 and adjusted R^2 values are 0.986 and 0.975 respectively, which is near to unity which confirms the adequacy of mode, Moreover, the adequate precision value is 24.8238 of ANOVA result. Figure 4.13 shows the plot of actual and predicted tensile strength. As represented in a table, the predicted R^2 is near to actual R^2. Thus, Figure 4.17 and R^2 value together represent that the developed model is accurate enough to predict the tensile strength. The derived forward regression mathematical model for tensile strength in terms of process parameters is shown by equation 4.3.

Tensile strength = 2757.1 - 2.29 × I - 41.2141 × S + 370.4629 × flux + 0.0425 × I × S - 0.93182 × S × flux + 0.142895 × S² - 57.329 × flux² (4.3)

Table 4.11 ANOVA analysis for tensile strength

| Source	Sum of Squares	Df	Mean Square	F-value	p-value	Source
Model	84427.46	7	12061.07	90.73	< 0.0001	significant
A-A	39480.5	1	39480.5	296.99	< 0.0001	
B-B	2485.23	1	2485.23	18.7	0.0019	
C-C	9508.98	1	9508.98	71.53	< 0.0001	
AB	1806.25	1	1806.25	13.59	0.005	
BC	1910.23	1	1910.23	14.37	0.0043	
B²	13794.11	1	13794.11	103.77	< 0.0001	
C²	9653.42	1	9653.42	72.62	< 0.0001	
Residual	1196.42	9	132.94			
Lack of Fit	1039.62	5	207.92	5.3	0.0655	not significant
Pure Error	156.8	4	39.2			
Cor Total	85623.88	16				
Std. Dev.	11.53		Adjusted R²	0.9752		
Mean	651.35		Predicted R²	0.9176		
C.V. %	1.77		Adequacy Precision	24.8238		
			R²	0.986		
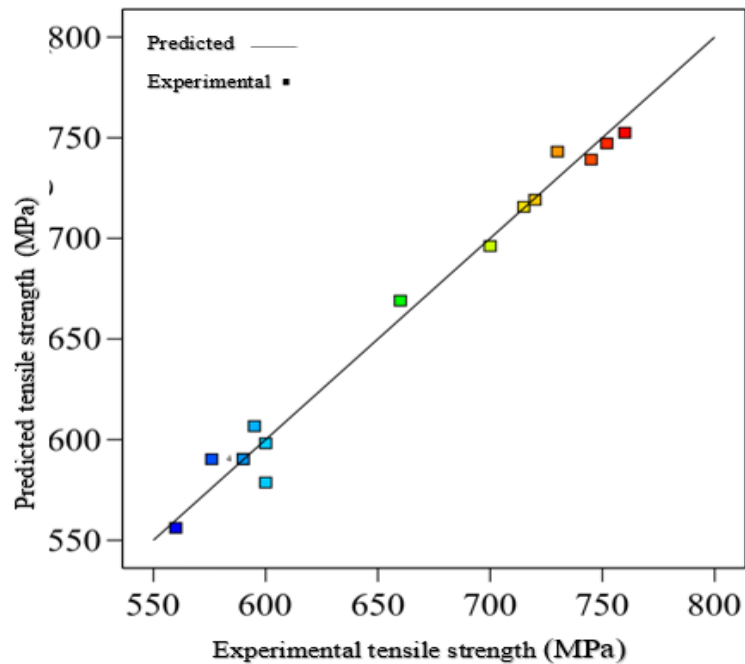
Figure 4.13 Schematics illustration of predicted values and experimental values agreement of tensile strength

4.4.4 Development of a mathematical model for Micro hardness

The ANOVA analysis for microhardness is shown in Table 4.12. The developed model of tensile strength has a p-value is less than 0.05. The F value of Lack of fit is found to be insignificant. The R^2 and adjusted R^2 value are 0.9888 and 0.9745 respectively, which is near to unity which confirms the adequacy of the model. Moreover, the adequate precision value is 25.2274 of the ANOVA result. Figure 4.14 shows the plot of actual and predicted tensile strength. As represented in a table, the predicted R^2 is near to the actual R^2. Thus, Figure 4.14 and R^2 value together represent that the developed model is accurate enough to predict the tensile strength. The derived quadratic mathematical model for microhardness in terms of process parameters is shown by equation 4.4.

$$\text{Microhardness} = 1027.7 - 5.92393 \times I - 5.86591 \times S + 217.4386 \times \text{flux} - 0.006 \times I \times S - 0.29273 \times I \times \text{flux} - 0.86591 \times S \times \text{flux} + 0.01776 \times I^2 + 0.03775 \times S^2 - 13.675 \times \text{flux}^2 \qquad (4.4)$$

Table 4.12 ANOVA analysis for microhardness

Source	Sum of Squares	df	Mean Square	F-value	p-value	Source
Model	7437.95	9	826.44	68.92	< 0.0001	significant
A-A	1985.52	1	1985.52	165.59	< 0.0001	
B-B	364.02	1	364.02	30.36	0.0009	
C-C	241.17	1	241.17	20.11	0.0029	
AB	36	1	36	3	0.1267	
AC	294.56	1	294.56	24.57	0.0016	
BC	1649.56	1	1649.56	137.57	< 0.0001	
A²	518.78	1	518.78	43.26	0.0003	
B²	960.04	1	960.04	80.06	< 0.0001	
C²	549.01	1	549.01	45.79	0.0003	
Residual	83.94	7	11.99			
Lack of Fit	19.14	3	6.38	0.3938	0.7651	not significant
Pure Error	64.8	4	16.2			
Cor Total	7521.88	16				

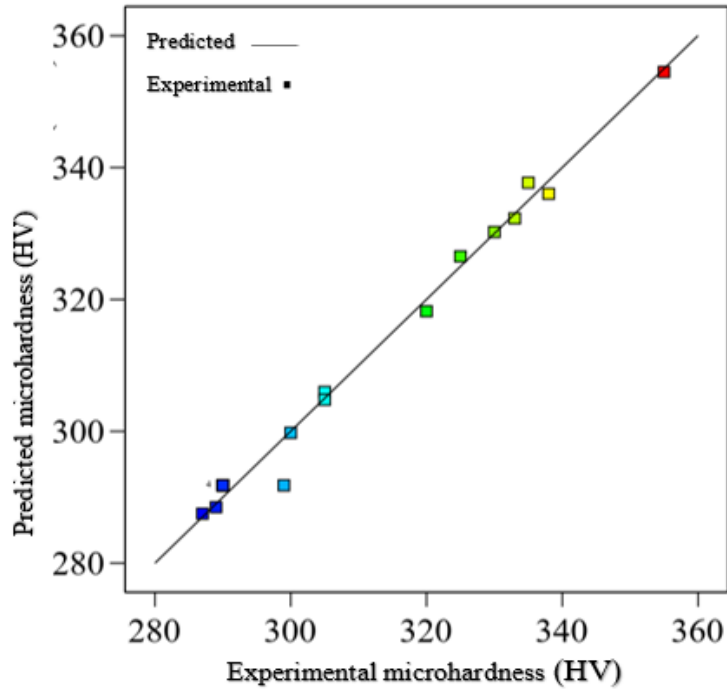| Std. Dev.	3.46	Adjusted R²	0.9745
Mean	310.65	Predicted R²	0.9203
C.V. %	1.11	Adequacy Precision	25.2274
		R²	0.9888

Figure 4.14 Schematics illustration of predicted values and experimental values agreement of microhardness

4.5 Effect of process variables on responses

For the responses weld depth, weld width, tensile strength and microhardness 3 D surface plots are shown in Figure 4.15- 4.18. In this surface plot, 1,2,3 represents the flux TiO_2, SiO_2 and Cr_2O_3 respectively. The effect of input variables such as welding current, torch speed and flux are shown along the X and Y axes and the response variable is shown on Z-axis that reveals the optimal level.

The interaction effect of input variables on the depth of penetration is shown in Figure 4.15 (a) - (c). As the current increase from 160 amps to 210 amps increases heat input and thereby penetration (Figure 4.15(a)). It is clearly observed form the interaction plots DOP proportionally increased with welding current and inversely proportional to torch speed

(Figure 4.13 (b)). Similar results were reported by Korra et al. (2014) and Tseng et al. (2012). Maximum depth of penetration is observed with SiO_2 flux compare to other two selected fluxes (Figure 4.15 (c)). This attributed to a difference in melting and boiling temperatures, density, composition and electro negativity between all considered fluxes.
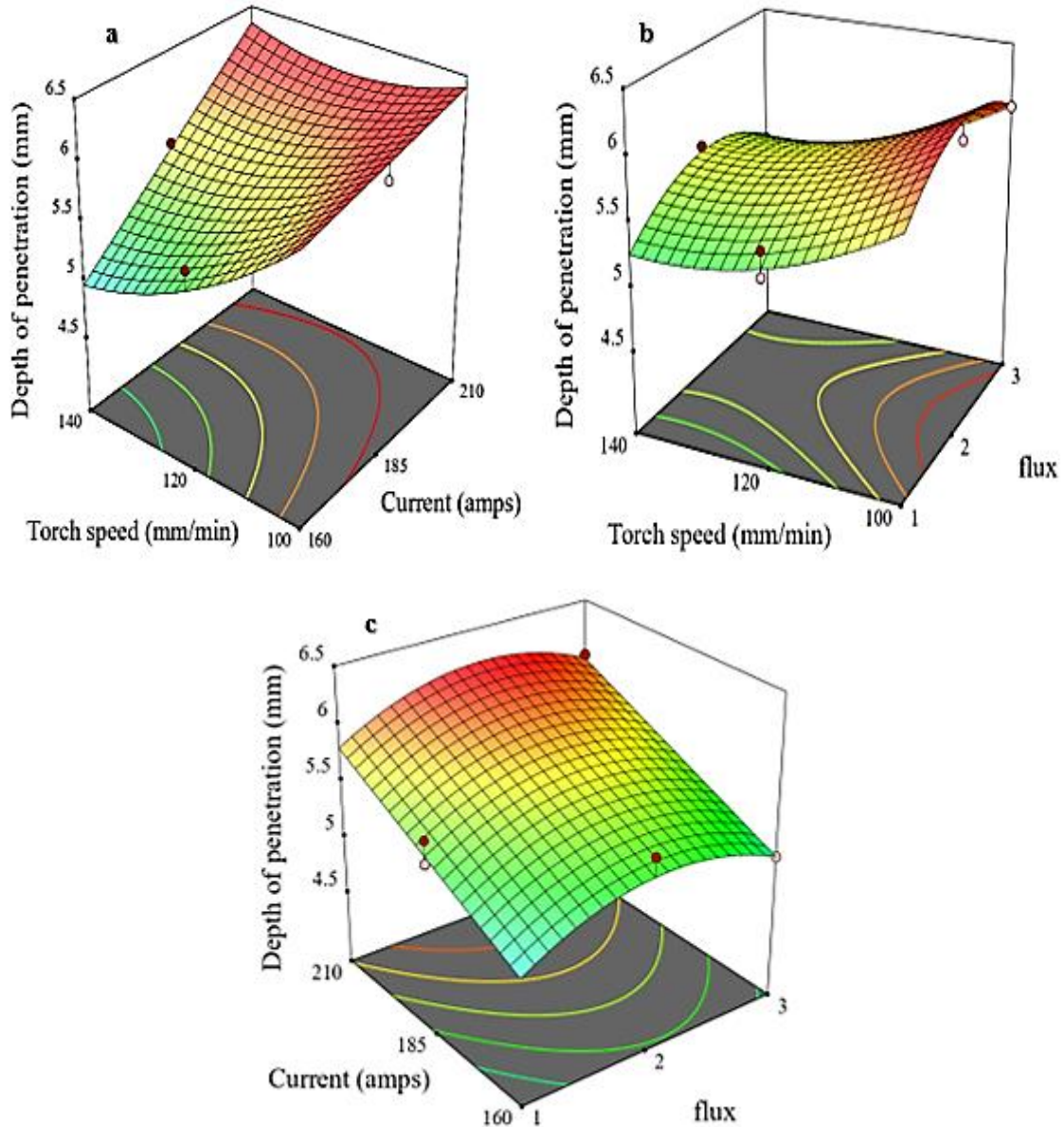

Figure 4.15 Illustration (a) effect of the current and torch speed on DOP (b) effect of the torch speed and flux on DOP (c) effect of the current and flux on DOP

Interaction effect of input variables on bead width is shown in

Figure 4.16 (a)- (c). At very high value of current 210 amps increase the penetration as shown in interaction plot Figure 4.14. However, it also increases the bead width as shown in Figure 4.15 (a). This is due to extra metal deposition on weld bead. It is

observed from the interaction plot Figure 4.15 (b), (c) that flux TiO_2 and Cr_2O_3 increase the bead width However, with SiO_2 flux minimum bead width is observed. This is due to strong interaction between the reversal Marangoni convection and arc constriction. Many research studies have also reported that with SiO_2 flux maximum D/W ratio is achieved in stainless steel (Tseng & Hsu, 2011). Among all considered parameters i.e. welding current, torch speed and flux, current and flux are dominating parameters over bead width, therefore, torch speed has comparably lesser influence on bead width.
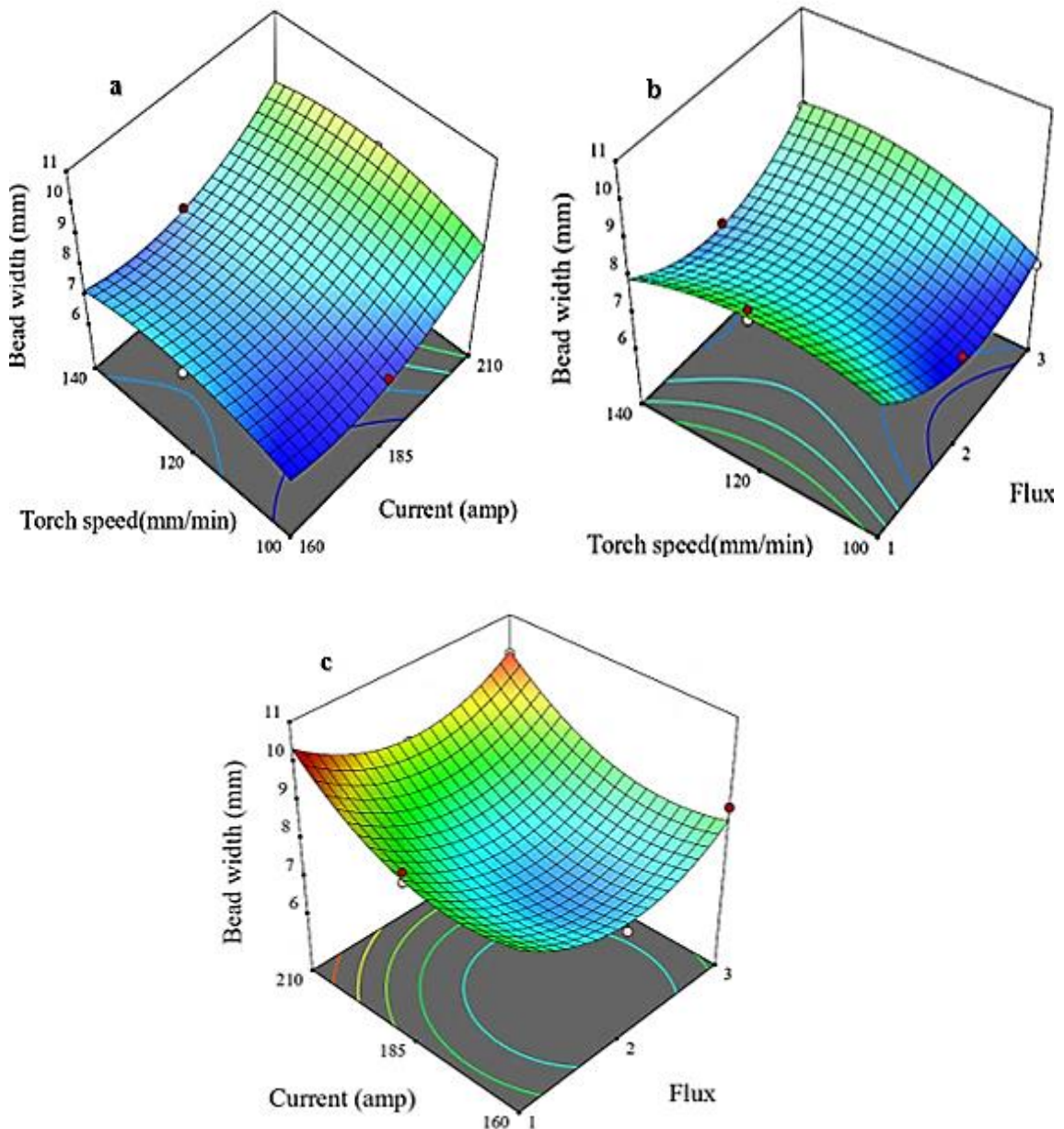

Figure 4.16 Illustration (a) effect of the current and torch speed on BW (b) effect of the torch speed and flux on BW (c) effect of the current and flux on BW

The interaction effect of welding current, torch speed and flux are shown in Figure 4.17(a)-(c). From the interaction, plots Figure 4.17(a), (b) it is observed that tensile strength is linearly increased with welding current but with torch speed, tensile strength is attained slightly higher at extreme edges. The high heat input may lead to lese ferrite formation along with growth of Widmannstetter structure in weld metal. This may increase the tensile properties of weld metal. Figure 4.17(c) shows the effect of fluxes on tensile properties of weld metal. The maximum tensile strength is reported with SiO_2 flux. The reason may be due to better ductility obtained with SiO_2 flux compared to the weld metal obtained with other two selected fluxes. A similar result was reported by Ramkumar et al. (2015) in 430 ferritic stainless steel.
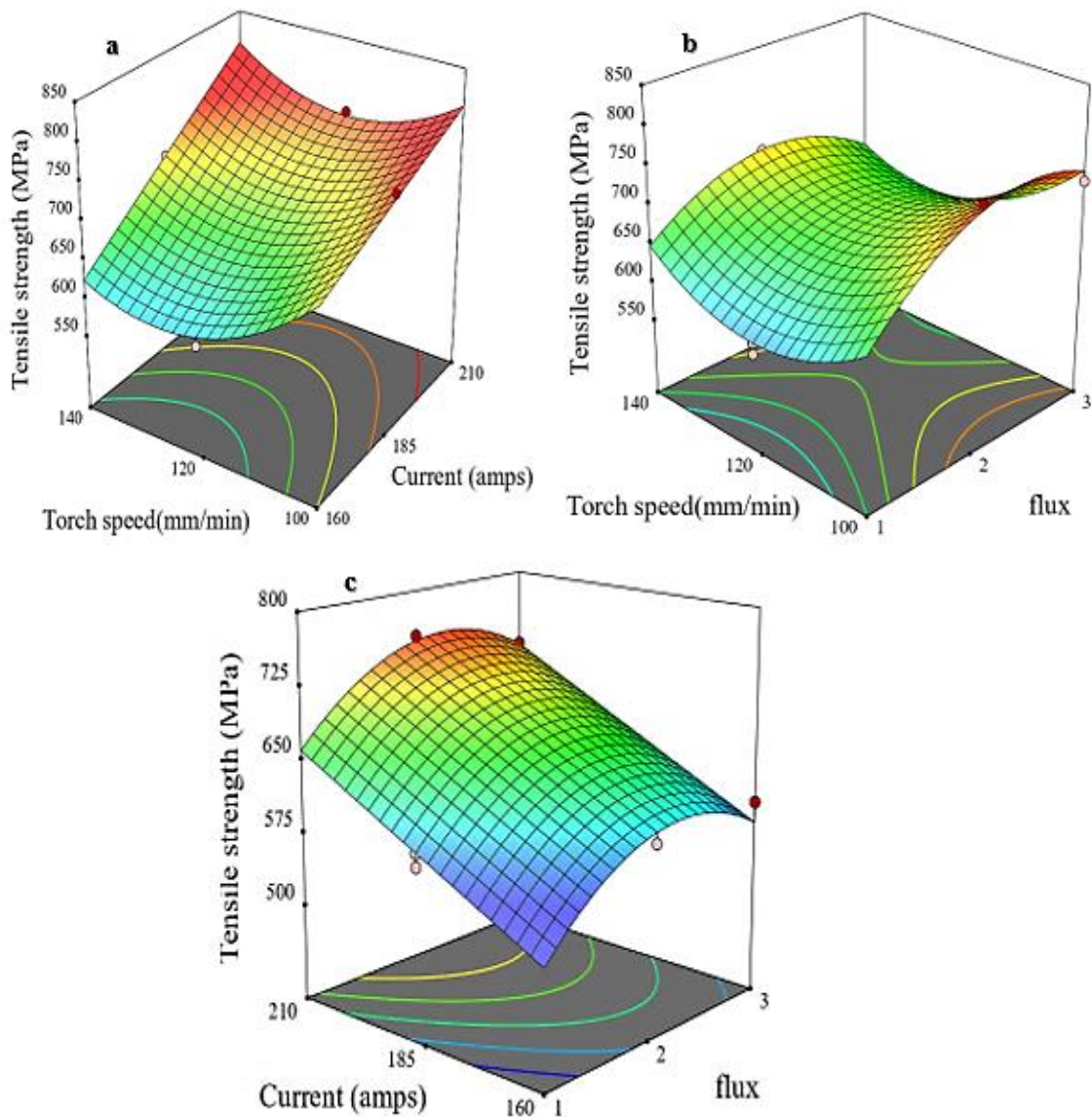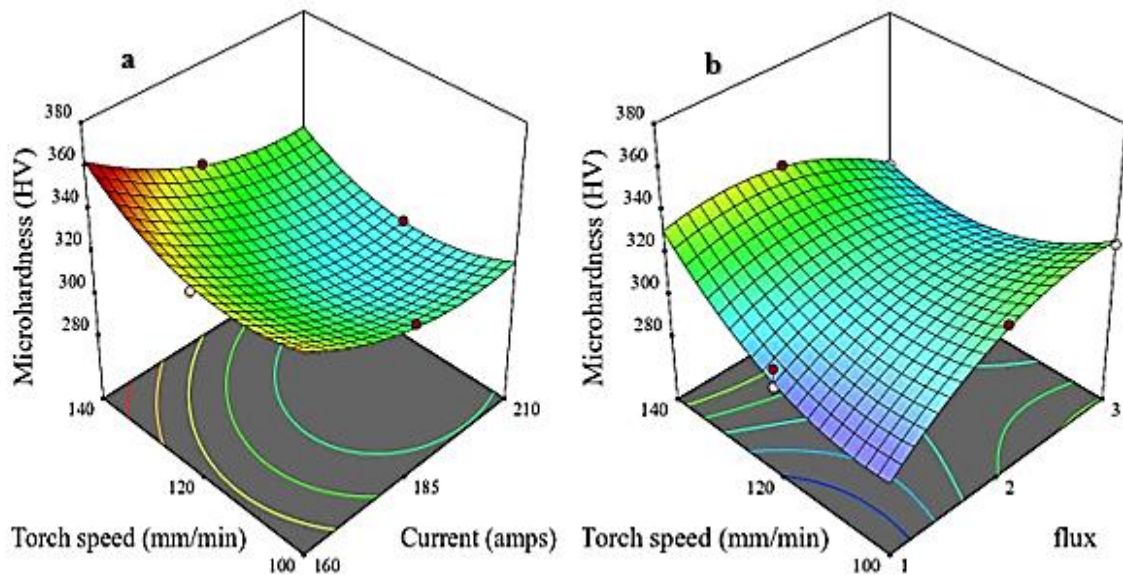

Figure 4.17 Illustration (a) effect of the current and torch speed on tensile strength (b) effect of the torch speed and flux on tensile strength (c) effect of the current and flux

on tensile strength

Figure 4.18 (a) – (c) shows the interaction effect of welding current, torch speed and flux on microhardness. It is observed from the surface plot Figure 4.18 (a), (b) that torch speed and welding current have almost equivalent influence on microhardness but reverses in nature. At low welding current 160 amps and higher torch speed 140 mm/min, lesser will be the heat input and higher microhardness this attributed to more delta ferrite formation in the weld metal. Similarly, at high welding current 210 amps and low torch speed 100 mm/min leads to very high heat input and thereby forming the less delta ferrite along with courser the grain structure. However, the maximum microhardness is reported with Cr_2O_3 flux as shown in Figure 4.18 (b), (c). This may due to the variation in cooling rate while using these fluxes.
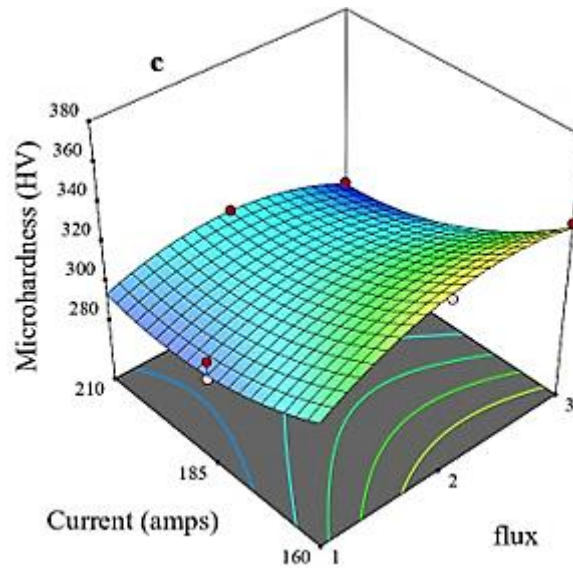
Figure 4.18 Illustration (a) effect of the current and torch speed on tensile strength (b) effect of the torch speed and flux on tensile strength (c) effect of the current and flux on tensile strength

4.6 Desirability approach in RSM

Derringer and Suich (1980) first proposed the desirability approach analysis technique. This method is used for several outputs into a dimensionless measure of performance. The desirability approach function converts each output into desirability function di (0≤i≤1) which varies from 0 to 1 (Montgomery, 2001). Few methods such as constrained optimization problems, overlaying the contour plots for each response and desirability approach are also being applied. However, the desirability approach is found simpler, flexible in weighting and giving importance to the individual response. Multi-objective optimization is performed using Design expert software in which the desirability function scale range varies from 0 to 1 to optimize the A-TIG weld parameters. Desirability 1 applies a more desirable response. Depending open the problem goal of the response is selected. The desirability function for each response can be calculated by the following equations concerning the target of the response (Korra, Vasudevan, & Balasubramanian, 2015).

For a goal of minimum, di =1 when Yi ≤ Lowi; di=1 when Yi ≥ Highi; and

$$di = \left(\frac{(High_i - Y_i)}{(High_i - Low_i)} \right)^{wt_i} \quad \text{when Low}_i < Y_i < High_i \qquad (4.5)$$

For a goal of maximization, di =1 when Yi ≥ Highi; and

$$di \; = \; \left(\frac{(Yi-Lowi)}{(Highi-Lowi)} \right)^{wti} \quad \text{when } Low_i < Yi < High_i \qquad (4.6)$$

For a goal as target di =1, when Yi < Lowi, and Yi > Highi

$$di \; = \; \left(\frac{(Yi-Lowi)}{(Ti-Lowi)} \right)^{wti} \quad \text{when } Low_i < Yi < High_i \qquad (4.7)$$

$$di \; = \; \left(\frac{(Yi-Highi)}{(Ti-Highi)} \right)^{wti} \quad \text{when } \; T_i < Yi < High_i \qquad (4.8)$$

Here i shows the response, Y the value of the response, T denotes the target value of the response, Low denotes the lower limit of the response, High denotes the upper limit of the response means the target values of the response, and wt indicates the weighted factor of the response which varies from 0.1 to 10. Wight value is unity exhibit the desirability function in linear mode. If it is greater than unity, gives more importance to the goal and if less than unity, gives less importance. To solve multi-response optimizations using the desirability approach combines multiple responses into a dimensionless measure of performance, this is known as overall desirability function (D) calculated by,

$$D \; = \; \left(II_{i=1}^{n} \; di_i^{ri} \right)^{1/\Sigma r} i \quad \text{when } \; T_i < Yi < High_i \qquad (4.9)$$

Where, number of responses mentioned with n in measure and importance (r) is given to each response, relative to the other responses which vary from 1 to 5. The higher value of desirability shows the more desirable function and is considered as the optimal solution.

4.7 Optimization and validation of optimum parameters

Multi-objective optimization is performed using the desirability approach in RSM. The purpose of optimization of the A-TIG welding process is to get the set of input variables for maximum depth of penetration, tensile strength and microhardness within the designated range of process parameters. The multiobjective optimization criteria used in this study are mentioned in Table 4.13. According to the criteria, the optimum solution is achieved with three sets of fluxes (TiO_2, SiO_2, Cr_2O_3) as shown in Table 4.14. As per the highest desirability values few observations are shown in a table with

all sets of fluxes. The optimized value of the process parameters for flux 2 (SiO_2) (welding current 201 amps, welding speed140 mm/min) results in higher tensile strength and depth of penetration than flux 1 and 3. This shall be articulated to better ductility obtained with SiO_2 flux compared to other two selected fluxes and strong reversal Marangoni convection with arc constriction. However, quite lesser microhardness is achieved with flux 2. Maximum microhardness is reported with Cr_2O_3 flux however the depth of penetration and tensile strength is drastically reduced. Therefore, the optimal solution is achieved with SiO_2 flux only as shown in table 9. The results are in good agreement with Ramkumar et al. (2015) and Chen et al. (2011).

Table 4.13 Criteria for optimization

Name	Goal	Limits		weight		Importance
		Lower Limit	Upper Limit	Lower Weight	Upper Weight	
Current (amps)	is in range	160	210	1	1	5
Torch speed (mm/min)	is in range	100	140	1	1	5
Flux	is equal to 1,2 and 3	1	3	1	1	5
DOP (mm)	maximize	4.5	6.13	0.1	1	5
BW (mm)	is in range	6.86	10.1	1	1	5
Tensile strength(MPa)	maximize	560	760	0.1	1	5
Microhardness (HV)	maximize	287	355	1	1	5

Table 4.14 Optimization results

Number	Current (amps)	Torch speed (mm/min)	DOP (mm)	BW (mm)	Tensile strength (MPa)	Micro hardness (HV)	Desirability
Flux 1 (TiO_2)							
1.	210	140	5.95	9.70	739.14	330.22	0.978

2.	208.85	140	5.92	9.58	734.95	329.78	0.976
3.	202.41	140	5.74	8.97	711.39	328.19	0.966
Flux 2 (SiO₂)							
1.	**201.86**	**140**	**6.13**	**7.90**	**777.38**	**324.22**	**0.983**
2.	203.3	140	6.17	8.18	770.64	324.00	0.98
3.	206.48	140	6.25	8.47	765.30	323.77	0.98
Flux 3 (Cr₂O₃)							
1.	162.01	100	5.85	6.99	698.07	354.99	0.982
2.	165.35	100	5.87	6.89	704.60	349.70	0.981
3.	174.45	100	5.93	6.79	722.45	337.25	0.979

The conformity experiment is performed on optimized process parameters when welding current is 201 amps, welding speed 140 mm/min and SiO_2 flux to check the conformity of the developed mathematical model. Weld macrostructure at optimum A-TIG weld parameters is shown in Figure 4.19. Moreover, by using equation 5 the percentage error is calculated. Actual values are in good agreement with the model predicted value as shown in Table 4.15.

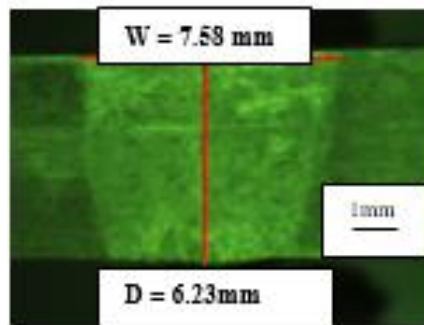$$Error \% = \frac{Actual\ value - Predicted\ value}{Predicted\ value} \times 100 \qquad (4.10)$$

Figure 4.19 Macrostructure of A-TIG weld metal observed in the confirmatory experiment

Table 4.15 Validation test result

Responses	DOP (mm)		Bead width (mm)		Tensile strength (MPa)		Microhardness (Hv)	
		Error %		Error %		Error %		Error %
Actual	6.23		7.58		775		322	
		1.7		4		0.30		0.6
Predicted	6.13		7.90		777.38		324.22	

At optimal parameters, Charpy impact test is performed to measure lateral expansion as per the standard procedure mentioned in chapter 3. Prepared specimens kept under the -29^0c temperature as shown in Figure 4.20 (a) followed by test. All three specimens fracture specimen (Figure 4.20 (b)) literal expansion is more than 0.38 mm which meet the ASME Section VIII Div. 1 requirement.

Figure 4.20 Charpy impact test (a) set up and (b) fractured impact test specimen

4.8 Summary

The summary of a systematic experimental investigation on a 6 mm thick 2205 DSS A-TIG weld joint is as follows.

The maximum D/W ratio of 0.87 is achieved with SiO_2 flux with 185 amps weld current and 100 mm/min torch speed. While in TIG weld joint under the same welding condition maximum D/W ratio 0.15 is obtained. TIG weld metal higher delta ferrite is observed compared to A-TIG weld metal this is due to higher cooling rate. The higher cooling rate results in to incomplete transformation from ferrite to the austenite. A higher value of tensile strength is observed in A-TIG weld joint compared to TIG weld joint. This is due to complete and secure penetration as well as less delta ferrite content formation. Along with

this, Widmannstetter structures with high miss-orientation of grain in A-TIG weld metal are responsible for high tensile strength. TIG (autogenous) weld microhardness is higher compared to all A-TIG weld metal. This is attributed to a large amount of ferrite formation in the weld metal.

The second-order mathematical model is developed by RSM for weld bead geometry and mechanical properties. The generated model is successfully used to predict the depth of penetration, bead width, tensile strength and microhardness for a given range of process variables in A-TIG welding. The most significant input variable is welding current, which has a prominent effect on weld bead geometry and tensile strength. The optimized parameter are 201amps welding current, 140 mm/min torch speed and SiO_2 flux at which 6.13 mm depth of penetration, 8.05 bead width, 777 MPa tensile strength and 320 HV microhardness are archived. Experimental validation of multi-objective optimization results indicate that the proposed optimization model is accurate enough to predict the responses of A-TIG welding process.